Broadband Dielectric and Resistivity Spectroscopy of $WO_3 \cdot H_2O$ in the Range of 10^3-10^{10} Hz: Particle Size Effect

L. Beluze,[†,‡] J. C. Badot,*[,†] R. Weil,[§] and V. Lucas[⊥]

Laboratoire de Chimie Appliquée de l'Etat Solide (LCAES), UMR CNRS 7574, ENSCP, 11 rue P. et M. Curie, 75231 Paris Cedex 05, France, Laboratoire de Réactivité et de Chimie des Solides, UMR CNRS 6007, Université J. Verne, 33 rue Saint-Leu, 80039 Amiens, France, Laboratoire de Génie Electrique de Paris (LGEP), UMR 8507, SUPELEC, Plateau de Moulon, 91192 Gif-sur-Yvette Cedex, France, and EADS CCR, 12 rue Pasteur BP 76, 92152 Suresnes Cedex, France

Received: October 26, 2005; In Final Form: February 27, 2006

The interest in studying the electrical properties of $WO_3 \cdot H_2O$ powders is made absolutely necessary because their infrared modulation properties depend on their morphologies and electronic populations. Broadband dielectric and resistivity spectra of $WO_3 \cdot H_2O$ powders were recorded in a frequency range of 10^3-10^{10} Hz at temperatures varying between 200 and 300 K. Complex resistivity and permittivity diagrams have permitted thermal behavior of both dc-conductivity and permittivity to be obtained. A dielectric relaxation is found, attributed to water molecules motions. The role of the powder morphology has been investigated on two types of compounds: the first one being constituted by nanometric particles and the second by micrometric particles. Strong differences are observed in the thermal behaviors of the dc-conductivities (activation energies). Particle size effect is evidenced, giving rise to stronger electron localization on the nanometric particles. The permittivity values and the dynamical behavior of the structural water are also influenced by the particle size effect. A strong interaction between moving polarons and water molecules has been determined.

I. Introduction

The recent interest in emissivity/reflectivity modulators was stimulated by the requisite control of the thermal exchange of a system without expending energy.[1−4] For example, this is of particular importance in satellite thermal control where heavy and expensive louver-type radiators (similar to venetian blinds) are used to regulate the radiation transfer. The development of plastic modulators is suitable to release from some technological constraints. So, the flexible devices could adjust to components with complex shapes, and their low weight would result in energy saving, especially for satellites. We recently reported the realization of a flexible emissivity modulator based on $WO_3 \cdot H_2O$ driven by the electrochemical insertion of lithium.[5−7] The injection of electrons comes with the insertion of small cations (typically H^+ or Li^+) in the compound. Hence, the variation in electron population can induce the change in optical behavior. Among all the compounds having electrochromic properties, tungsten trioxide (WO_3) presents a contrast not only in the visible range but also in the infrared range. However, tungsten trioxide monohydrate ($WO_3 \cdot H_2O$) has been chosen because the cation diffusion coefficient is high, owing to the presence of water molecules between tungsten trioxide sheets.[8] Consequently, this electrochromic compound commutes faster than WO_3. A previous paper has demonstrated that $WO_3 \cdot H_2O$ powder embedded in a plastic matrix could be used as the active component in the $LiCoO_2$/lithium electrolyte/$WO_3 \cdot H_2O$ system. The reflectivity of the powder was strongly influenced by the particles morphology. Two elaboration methods (Freedman[9] and Furusawa[10] methods) were used, leading to very different shapes and sizes of particles (grains). SEM micrographs of the $WO_3 \cdot H_2O$ powder[6] obtained by the Freedman method reveal nanometric parallelepiped-shaped grains. A completely different microstructure with larger micrometric platelet-shaped grains was achieved with the Furusawa method. The larger grain size of the Furusawa powder was found to induce a larger improvement in IR modulation properties.[6] $WO_3 \cdot H_2O$ exhibits a layered orthorhombic structure with the *Pnmb* space group (Figure 1). The lattice parameters are $a = 5.247$ Å, $b = 10.712$ Å, and $c = 5.137$ Å. The structure consists of sheets of distorted octahedral units of tungsten atoms coordinated by five oxygen atoms and a water molecule. The sheets are linked by hydrogen bonding between the water molecules and the neighboring oxygen atoms of the adjacent layer. Lithium ions can thus easily intercalate between the tungsten trioxide sheets.

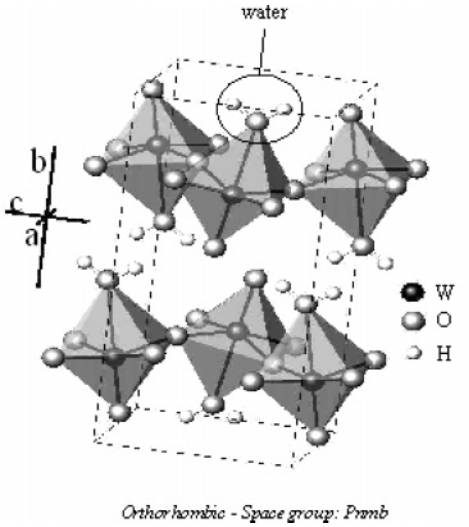

Figure 1. Schematic representation of the $WO_3 \cdot H_2O$ orthorhombic unit cell.[6]

The study of intrinsic electrical properties becomes difficult since $WO_3 \cdot H_2O$ is obtained in powder form. So, when the

* Corresponding author. E-mail: jc-badot@enscp.fr.
† Laboratoire de Chimie Appliquée de l'Etat Solide.
‡ Laboratoire de Réactivité et de Chimie des Solides.
§ Laboratoire de Génie Electrique de Paris.
⊥ EADS CCR.

10.1021/jp0561524 CCC: $33.50
Published on Web 03/24/2006

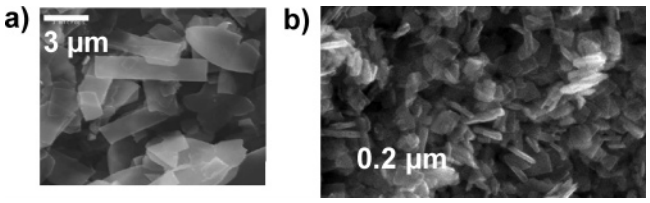

Figure 2. SEM micrographs[6] of $WO_3 \cdot H_2O$ powders obtain by (a) Furusawa (WFU) and (b) Freedman (WFR) procedures.

materials are polycrystalline (compacted or sintered powders, thin films, etc.) the conductivity measurements by the usual dc techniques cannot provide any information on the electrical transport properties owing to the complexity of their microstructures and/or nanostructures. On the other hand, ac techniques (up to microwave frequency range) are powerful tools for the electrical characterization of polycrystalline materials. These techniques probe the interaction of a material with a time-dependent electric field. The response is either expressed by the frequency-dependent complex permittivity ϵ, conductivity σ, or resistivity ρ. The resulting charge density fluctuations are generally described by relaxations up to millimeter wavelengths. The time scale (or relaxation time) of these fluctuations depends on the sample and on the relevant relaxation mechanism. In inorganic compounds, these fluctuations generally arise from the reorientation of dipolar species (e.g., water in hydrates such as $V_2O_5 \cdot 1.6H_2O$, $HUO_2PO_4 \cdot 4H_2O$, etc.) or from the charge local hopping (e.g., ions, protons, and/or polarons) at higher frequencies. Other possible mechanisms include the appearance of interfacial charge fluctuations (e.g., polarization reversal due to grain boundaries) at lower frequencies.

In the present paper, we report the first detailed study concerning the broadband dielectric (or resistivity) spectroscopy of $WO_3 \cdot H_2O$ compounds obtained by both the Freedman[9] and Furusawa[10] methods, which will be hereafter called WFR and WFU, respectively. The spectra were recorded within the temperature range 200 to 300 K. The influence of a particle size will also be discussed in order to understand the electrical dielectric properties of $WO_3 \cdot H_2O$.

II. Experimental SectionProcedures

Synthesis of $WO_3 \cdot H_2O$ and Structural Characterizations. The $WO_3 \cdot H_2O$ powders were synthesized according to two methods as has been described in previous papers.[6,9,10] The first one (the Furusawa method[10]), which is a crystal-growth method based on a sol−gel route, allows for platelet-shaped particles (crystallites) with sizes about $3000 \times 5000 \times 40$ nm^3 (Figure 2a) to be obtained. The second (Freedman method[9]), which is based on a rapid precipitation of the compound, yields smaller parallelepiped shaped particles (crystallites) with sizes about $120 \times 120 \times 40$ nm^3 (Figure 2b). Particle sizes have been determined by scanning electron microscopy (SEM). SEM micrographs[6] were obtained with a Philips FEG (field effect gun) XL 30 microscope for WFR powder and with a Hitachi S2500 microscope for WFU powder.

Permittivity and Resistivity Measurements. Complex resistivity and permittivity spectra were recorded over a broad frequency range of 10^3 to 10^{10} Hz, using simultaneously two network analyzers HP 8751 (from 10^3 to 10^8 Hz) and HP 8510 (from 4.5×10^7 to 10^{10} Hz). The experimental device, fully described in previous papers,[11,12] consists of a coaxial cell (APC7 standard) in which the cylindrically shaped sample (radius = 1.5 mm and thickness = 1 mm) with silver plated front faces fills the gap between the inner conductor and a short

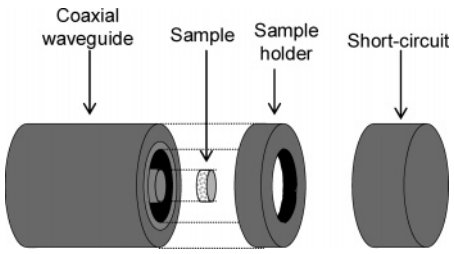

Figure 3. Schematic coaxial line (APC7 standard) used to measure permittivity and resistivity of materials.

circuit (Figure 3). After a relevant calibration of the analyzers, the sample admittance Y_s is computed from measurements of the complex reflection coefficient of the device. The knowledge of Y_s allows us to determine the complex (relative) permittivity $\epsilon(\omega) = \epsilon'(\omega) - i\epsilon''(\omega)$ of the sample according to the equation

$$Y_s = i\frac{k_s r_s}{\nu \mu_0 d_s}\frac{J_1(k_s r_s)}{J_0(k_s r_s)} \quad (1)$$

where $i = (-1)^{1/2}$, μ_0 is the free space permeability, $\nu = \omega/2\pi$ is the frequency (in Hz), $k_0 = \omega/c$ ($c = 3 \times 10^8$ m·s^{-1}), and $k_s = k_0(\epsilon(\omega))^{1/2}$. r_s and d_s are the radius and the thickness of the sample, respectively. J_0 and J_1 are zero- and first-order Bessel functions of the first kind, respectively. Expression 1 is only available when the inequality $d_s \cdot \mathrm{Re}[(\epsilon(\omega))^{1/2}] < \pi c/\omega$ is fulfilled, $\mathrm{Re}[(\epsilon(\omega))^{1/2}]$ being the real part of $(\epsilon(\omega))^{1/2}$. Complete dielectric spectra were made from about 400 measurements with an accuracy of approximately 3% to 5% in the whole frequency range. The knowledge of the complex permittivity allows the calculation of the complex resistivity $\rho = \rho' - i\rho'' = (i\omega\epsilon_0\epsilon)^{-1}$ (ϵ_0 being the vacuum permittivity). The samples are compacted powders and the measurements were made in the range 200 to 300 K under dry N_2 flux.

III. Results and Discussion

The frequency dependence of the real and imaginary parts ϵ' and ϵ'' of WFU and WFR permittivity ϵ are shown in Figure 4 at 283 K. All dielectric spectra are similar whatever the temperature of the samples. The real part of the permittivity ϵ' vs frequency decreases by about 2 to 3 orders of magnitude from 10^3 to 10^{10} Hz (Figure 4a). For frequencies around 10^3 Hz, the values of ϵ' are between 10^3 and 2×10^4, which indicates a strong capacitive effect due to interfacial polarization (e.g., grain boundaries). On the other hand, dielectric losses ϵ'' vs frequency (Figure 4b) vary by about 3 to 4 orders of magnitude from 10^3 to 10^{10} Hz.

As the relaxations are not clearly shown in dielectric spectra, the use of Nyquist plots for complex parameters (ρ'' vs ρ' and ϵ'' vs ϵ') is helpful. To provide evidence for the different relaxations we used a decomposition procedure of the Nyquist plot, which has been described elsewhere.[11,13] The complex resistivity plots are useful to determine the grain bulk dc-conductivity in powdered compounds (compacted or sintered). Figure 5 shows the entire complex resistivity diagram, $\rho'' = f(\rho')$ of WFU at 283 K. In the low-frequency part of the graph, the first dispersion domain 1 is well fitted by a circular arc. The later corresponds to resistivity relaxation described by the following complex function:

$$\rho(\omega) = \rho_H + \frac{\rho_L - \rho_H}{1 + (i\omega\tau_\rho)^{1-\alpha}} \quad (2)$$

where ρ_L and ρ_H are respectively the low- and high-frequency

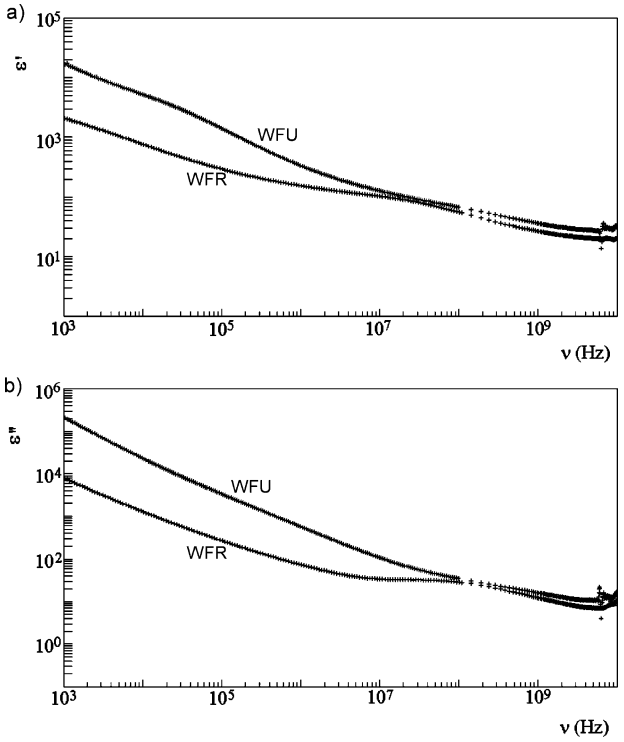

Figure 4. Dielectric spectra of $WO_3 \cdot H_2O$ samples obtained by Freedman (WFR) and Furusawa (WFU) procedures: (a) real part ϵ' and (b) imaginary part ϵ'' of the permittivity vs frequency ν ($\nu = \omega/2\pi$) at $T = 283$ K.

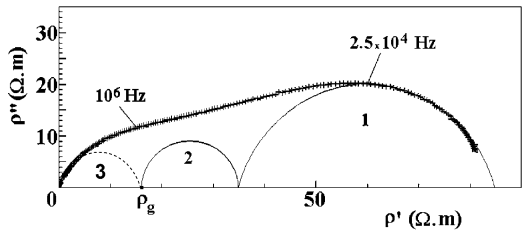

Figure 5. Plot of the imaginary part $\rho''(\omega)$ versus the real part $\rho'(\omega)$ of the complex resistivity at 283 K for WFU. $\omega/2\pi$ is the frequency expressed in hertz.

limits of the resistivity, τ_ρ is the relaxation time, and α is a fitting parameter. The two relaxation domains 2 and 3, which are represented by two circular arcs, are plotted after subtracting the contributions of domains 1 and 2, respectively. Since the high-frequency part of domain 3 crosses the origin, it corresponds to the bulk (grain) contribution. Domain 2 is due to contact resistances and capacitances between the grains. The lower frequency domain 1 is thus due to contact resistances and capacitances between the sample and the silver electrodes. The silvered samples are similar to a series of three impedances (grain bulk, grain boundary, and interface silver/sample), each of them being associated with a parallel combination of resistance and capacitance. It is then possible to obtain the grain bulk dc-conductivity $\sigma_g = (\rho_g)^{-1}$ from the only intersection of domains 2 and 3 with the real ρ'-axis. All complex resistivity diagrams are similar whatever the temperature and the compound. Is $WO_3 \cdot H_2O$ an electronic or a protonic conductor? A previous paper has shown that no proton transport by the bulk mechanism can be expected because there is no interlayered water (or free-water).[14] $WO_3 \cdot H_2O$ can be compared with m-WO_3,[15] in which small polarons contribute predominantly to electrical transport as majority carriers. We can thus suggest the existence of oxygen vacancies, compensated by excess

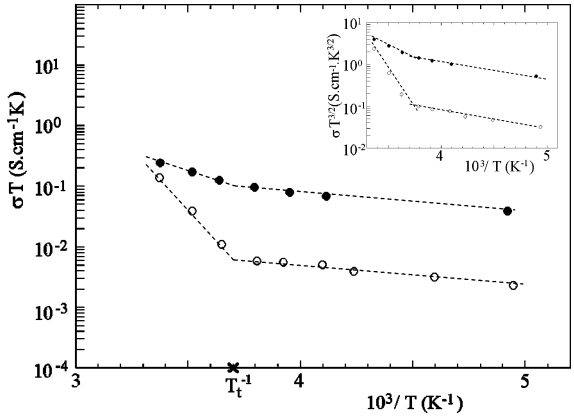

Figure 6. Bulk dc-conductivity σ_g as a function of inverse temperature T^{-1} ($\log\sigma T$ vs T^{-1}) for WFU (●) and WFR (○). $T_t \approx 268$ K is the transition temperature between low- and high-temperature regimes. The inset plot corresponds to the temperature dependence, $\log\sigma T^{3/2}$ vs T^{-1} for WFU (●) and WFR (○).

electrons, reducing W^{6+} into W^{5+} and contributing to the electronic conductivity in $WO_3 \cdot H_2O$. The electrons are localized on tungsten sites associated with oxygen vacancies leading to the formation of "bound-polarons". Since the sheets are separated by water molecules, the conducting pathways are disrupted along the *b*-axis of the structure: the conductivity of $WO_3 \cdot H_2O$ having thus a two-dimensional aspect. Figure 6 shows the resulting temperature dependence of σ_g for both compounds WFU and WFR. Two conductivity regimes (high and low temperature) are evidenced with the same transition temperature $T_t \approx 268$ K and have thermally activated behaviors as

$$\sigma_g = A_i T^{-n} \exp\left(\frac{E_i}{kT}\right) \tag{3}$$

with $n = 1$ or $^3/_2$ for adiabatic (A) or nonadiabatic (NA) polaron hopping, respectively. E_i is the activation energy for low (i = LT) or high temperature (i = HT). These preliminary data analyzed herein are not sufficiently precise to distinguish between the two types of small-polaron conduction mechanism (adiabatic or nonadiabatic). For $T < T_t$, the conductivities of both compounds have the same activation energy $E_{LT}(A) \approx 0.08$ eV or $E_{LT}(NA) \approx 0.09$ eV. On the other hand, for $T > T_t$, the activation energies E_{HT} are strongly different: (i) for WFU, $E_{HT}(A) \approx 0.19$ eV or $E_{HT}(NA) \approx 0.20$ eV, and (ii) for WFR, $E_{HT}(A) \approx 0.79$ eV or $E_{HT}(NA) \approx 0.80$ eV. While the high-temperature activation energy E_{HT} for WFU corresponds to that observed for WO_3,[15] the value of E_{HT} for WFR seems to be abnormally high. This difference can only be explained by a size effect. The small crystallites of WFR are in the nanometric size range, as commented above. In this case, the surface effects on charge carriers are increased. As a result, localized states become possible at the surface because the electrons are strongly trapped there. The region of the semiconductor close to the surface is then depleted of its electrons: it is called a depletion region,[16] which is positively charged. This nonuniform charge distribution (space-charge) induces an electric field that is opposed to the electronic transport. The conduction is only possible for the electrons (polarons) which are able to jump over a supplementary barrier height, i.e., $\delta E_{HT} = 0.60$ eV in WFR.

For $T > T_t$, the conduction is predominantly due to free charge carriers (small polarons) thermally excited from donors (oxygen vacancies) in both compounds. For $T < T_t$, the transport of charge carriers is governed by impurity conduction, which

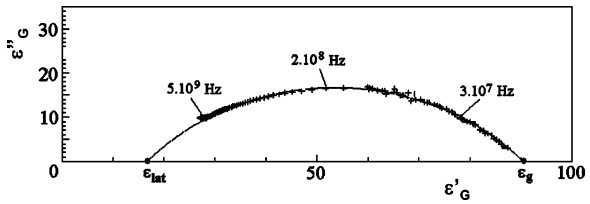

Figure 7. Cole−Cole plot of the imaginary part $\epsilon_G''(\omega)$ vs the real part $\epsilon_G'(\omega)$ of the complex permittivity $\epsilon_G(\omega)$ at $T = 283$ K for WFU. The contributions of the dc-conductivity and the interfacial (grain boundaries and Ag/sample interfaces) polarizations have been subtracted.

corresponds to the transfer from an occupied to a neighboring unoccupied donor. This transport can be described by a two-step process: (i) the first one consists of extracting the electron from the electrostatic field of the defect (oxygen vacancy)[17] with a probability proportional to $\exp(-E_{LT}/kT)$ while (ii) the second is a tunneling transfer to a neighboring site.[17,21] The value of the transition temperature $T_t = 0.3\hbar\omega_{ph}/k$ ($\omega_{ph} \approx 1.26 \times 10^{14}$ s^{-1} being the optical phonon frequency[6]) lies in the range 0.25 to 0.5 $\hbar\omega_{ph}$ as previously shown in polaron Holstein theory.[19,20] Figure 6 shows that the low-temperature conductivity of WFR is about 10 times lower than that in WFU. That is due to a lower number of mobile polarons in WFR, as a consequence of a higher electronic depletion, involving a higher content of ionized donors (oxygen vacancies) in the grain bulk.

Otherwise, if the resistivities due to interfacial and grain boundary polarizations (domains 1 and 2) (Figure 5) are subtracted from the sample resistivity $\rho(\omega)$, the grain bulk resistivity is

$$\rho_G(\omega) = \rho(\omega) - \frac{\rho_1 - \rho_2}{1 + (i\omega\tau_1)^{1-\alpha_1}} - \frac{\rho_2 - \rho_g}{1 + (i\omega\tau_2)^{1-\alpha_2}} \quad (4)$$

where τ_1 and τ_2 are the relaxation times of domains 1 and 2, respectively. The grain bulk complex permittivity $\epsilon_G = (i\omega\epsilon_0\rho_G)^{-1}$ is obtained as a function of the frequency. The dielectric spectra of the grain bulk under the form of a Cole−Cole plot (Figure 7), i.e., $\epsilon'' = f(\epsilon')$, has revealed only one dielectric relaxation well fitted by the Cole−Cole expression,

$$\epsilon_G(\omega) = \epsilon_\infty + \frac{\epsilon_g - \epsilon_\infty}{1 + (i\omega\tau)^{1-\alpha}} \quad (5)$$

after subtraction of the contribution $\sigma_g/\epsilon_0\omega$ of the grain dc-conductivity. ϵ_g and ϵ_∞ are respectively the low- and high-frequency limits of the permittivity. Note that ϵ_g is the static permittivity of the grain (particle). τ is the relaxation time and α is a fitting parameter that is here equal to 0.5 whatever the temperature and the sample. Figure 8 shows the relaxation frequency ν_w observed in WFU with a constant value $\nu_w = \nu_{w0} = 2 \times 10^8$ Hz whatever the temperature. Since the activation energy is equal to zero, the water molecules rotate without breaking hydrogen bonds. We may thus suggest that they perform oscillations similar to cooperative "windscreen wiper" motions. The relaxation frequency of water motion in WFR varies slightly with the temperature. It could be described by an Arrhenius law, $\nu_w = \nu_0 \exp(-E_w/kT)$, with a low activation energy $E_w \approx 0.03$ eV. The prefactor ν_0 has the same value as the water relaxation frequency in WFU, i.e., $\nu_0 = \nu_{w0} = 2 \times 10^8$ Hz. The activation energy E_w is of the order of kT, which corresponds to the value of the "ion−mobile dipole" interaction.[22,23] It is obvious to consider that the positively charged depletion region gives rise to the same type of interaction in

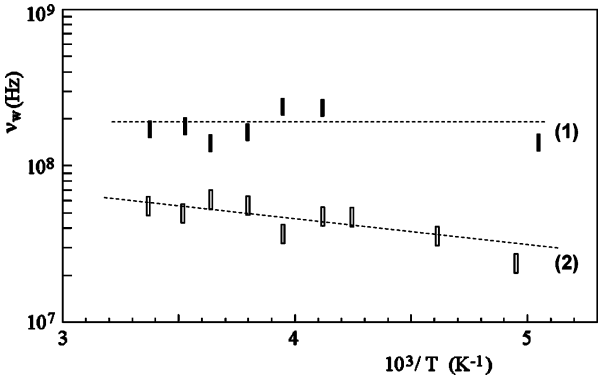

Figure 8. Inverse temperature dependence of the relaxation frequency of structural water motion in WFU (1) and WFR (2).

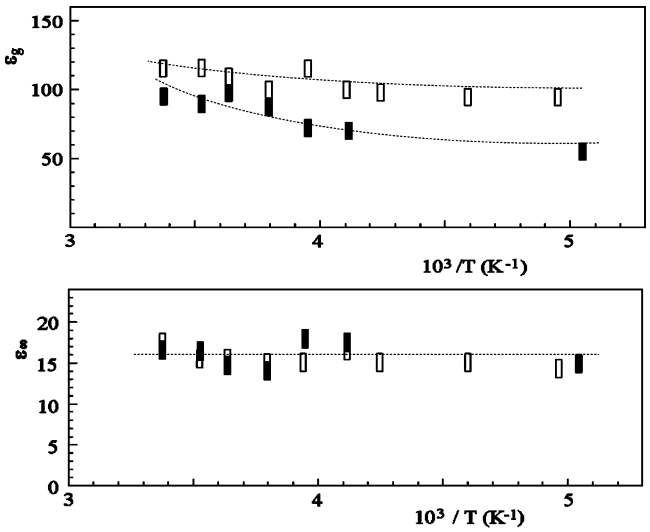

Figure 9. Temperature dependence of low- and high-frequency limits of the permittivity: (a) ϵ_g and (b) ϵ_∞ respectively for WFU (■) and WFR (□).

WFR. The water molecules (dipoles) are aligned by the electrostatic field created by the positive charges. This alignment involves a higher polarization, i.e., a higher value of ϵ_g for WFR (Figure 6). Moreover, the high values of ϵ_g (Figure 9a) would be due to the existence of an antiferroelectric order of H_2O dipoles, since they are antiparallel (Figure 1). The existence of this antiferroelectric order is corroborated by the decrease of ϵ_g with decreasing temperature. Note that a high permittivity could thus favor a depletion layer width,[16]

$$d = \left(\frac{2\epsilon_0\epsilon_g\delta E_H}{e^2 N_D}\right)^{1/2} \quad (6)$$

larger than the grain size d_g in WFR. N_D is the doping (oxygen vacancy) content because d is given as a function of δE_H, ϵ_g, and doping content N_D (here, oxygen vacancies content). The permittivity $\epsilon_\infty \approx 16$, which is not dependent on the particle size and the temperature (Figure 9b), corresponds to the lattice (vibrations) and electronic contributions of the polarizability.

We may anticipate that lithium ions will tend to segregate on the nanoparticle surface. Consequently, insertion and deinsertion of lithium ions would be faster, since diffusion on the particle surface requires lower energy than that in the particle bulk. This hypothesis agrees with experimental evidence of a better reversibility of Li insertion−deinsertion for the nanometric powder after several electrochemical cycles.[6] However, further dielectric and resistivity spectroscopic measurements on the

lithiated compounds $Li_xWO_3H_2O$ have to be performed to establish a more precise correlation between the infrared modulation and the electrical properties depending on the lithium insertion.

IV. Conclusions

Dielectric and resistivity spectroscopy from 10^3 to 10^{10} Hz has allowed the determination of electrical transport properties of $WO_3 \cdot H_2O$ compacted powders in the temperature range 200−300 K. Interpretation of the spectra was made possible through the knowledge of the micro- and nanostructures previously studied by scanning electron microscopy. A combination of complex resistivity and permittivity diagrams has allowed the determination of the electrical behavior with the temperature. Resistivity relaxations are attributed to interfacial and grain boundary polarization phenomena in the samples. Bulk dc-conductivities of $WO_3 \cdot H_2O$ powders were obtained vs temperature by taking into account the interfacial phenomena. Strong differences are observed in the thermal behavior of the dc-conductivities. Indeed, at temperatures higher than 268 K, the conductivities are thermally activated with different activation energies, equal to 0.19 and 0.79 eV for micrometric and nanometric powders, respectively. The particle size effect has been evidenced, giving rise to stronger electron (small polaron) localization on the particle surface and higher activation energy for the nanometric particles. In the higher frequency range ($\approx 10^8$ Hz), a dielectric relaxation was evidenced and attributed to structural water motions. These rotational motions are also influenced by the size effect. Accordingly, the existence of an electrostatic field created by a charge-space in the nanometric particles has induced a slowing-down of the water molecule's motions. We have evidenced a strong interaction between moving small polarons and water molecules in a hydrate. The size effect acts on the electronic transport in $WO_3 \cdot H_2O$, because its high permittivity of $\epsilon_g \approx 100$ is the result of an antiferroelectric order of the H_2O dipoles.

Acknowledgment. The authors thank Prof. N. Baffier (LCAES, Paris), Prof. A. Kreisler (LGEP, Gif-sur-Yvette), Prof. J. M. Tarascon (LRCS, Amiens), and Dr. B. Viana (LCAES, Paris) for their interest in the work and EADS for financial support.

References and Notes

(1) Granqvist, C. G. In *Materials Science for Solar Energy Conversion Systems*; Pergamon Press: Elmsford, NY, 1991.
(2) Cogan, S. F.; Rauth, R. D.; Westwood, D.; Plottkin, D. I.; Jones, R. B. *Proc. SPIE* **1989**, 2.
(3) Hale, S. J.; De Vries, M.; Dworak, B.; Woolam, J. A. *Thin Solid Films* **1998**, *313*−*314*, 205.
(4) Trimble, C.; Franke, E.; Hale, J. S.; Woolam, J. A. *Thin Solid Films* **1999**, *355*−*356*, 617.
(5) Bessière, A.; Marcel, C.; Morcrette, M.; Tarascon, J. M.; Lucas, V.; Viana, B.; Baffier, N. *J. Appl. Phys.* **2002**, *91*, 1589.
(6) Bessière, A.; Beluze, L.; Morcrette, M.; Lucas, V.; Viana, B.; Badot, J. C. *Chem. Mater.* **2003**, *15*, 2577.
(7) Bessière, A.; Beluze, L.; Morcrette, M.; Viana, B.; Frigerio, J. M.; Andraud, C.; Lucas, V. *J. Appl. Phys.* **2004**, *95* (12), 7701.
(8) Judeinstein, P.; Livage, J. *Mater. Sci. Eng.* **1989**, *B3*, 129.
(9) Freedman, M. L. *J. Am. Chem. Soc.* **1959**, *81*, 3834.
(10) Furusawa, K.; Hachisu, S. *Sci. Light* **1966**, *15* (2), 115.
(11) Ragot, F.; Badot, J. C.; Baffier, N.; Fourrier-Lamer, A. *J. Mater. Chem.* **1995**, *5*, 1155.
(12) Badot, J. C.; Bianchi, V.; Baffier, N.; Belhadj-Tahar, N. *J. Phys.: Condens. Matter* **2002**, *14*, 6917.
(13) Rotenberg, B.; Cadène, A.; Dufrêche, J.-F.; Durand-Vidal, S.; Badot, J.-C.; Turq, P. *J. Phys. Chem. B* **2005**, *109*, 15548.
(14) Li, Y. M.; Hibino, M.; Miyayania, M.; Kudo, T. *Solid State Ionics* **2000**, *134*, 271.
(15) Iguchi, E.; Miyagi, H. *J. Phys. Chem. Solids* **1993**, *54* (4), 403.
(16) Bube, R. H. In *Electrons in Solids*; Academic Press: New York, 1981.
(17) Sanchez, C.; Henry, M.; Grenet, J. C.; Livage, J. *J. Phys. C*: *Solid State Phys.* **1982**, *15*, 7133.
(18) Alexandrov, A. S.; Mott, N. In *Polarons and Bipolarons*; World Scientific: Singapore, 1998.
(19) Holstein, T. *Ann. Phys. N.Y.* **1959**, *8*, 343.
(20) Bosman, A. J.; van Daal, A. J. *Adv. Phys.* **1970**, *19*, 1.
(21) Thorn, R. J. *Physica C* **1992**, *190*, 193.
(22) Gerschel, A. In *Liaisons intermoléculaires*; Interéditions/CNRS Editions, 2000.
(23) Butt, H. J.; Graf, K.; Kappl, M. In *Physics and Chemistry of Interfaces*; Wiley-VCH GmbH: Weinheim, Germany, 2003.